A thermodynamic framework for ductile phase-field fracture and gradient-enhanced crystal plasticity

Citation for the original published paper (version of record):
Auth, K., Brouzoulis, J., Ekh, M. (2024). A thermodynamic framework for ductile phase-field fracture and gradient-enhanced crystal
plasticity. European Journal of Mechanics, A/Solids, 108.
http://dx.doi.org/10.1016/j.euromechsol.2024.105418

European Journal of Mechanics / A Solids 108 (2024) 105418

Contents lists available at ScienceDirect

European Journal of Mechanics / A Solids

journal homepage: www.elsevier.com/locate/ejmsol

Full length article

A thermodynamic framework for ductile phase-field fracture and gradient-enhanced crystal plasticity

Kim Louisa Auth [a,*], Jim Brouzoulis [b], Magnus Ekh [a]

[a] Division of Material and Computational Mechanics, Department of Industrial and Materials Science, Chalmers University of Technology, 41296, Sweden
[b] Division of Dynamics, Department of Mechanics and Maritime Sciences, Chalmers University of Technology, 41296, Sweden

ARTICLE INFO

Keywords:
Phase-field fracture
Ductile
Gradient-enhanced plasticity
Crystal plasticity
Staggered solution scheme
Micromorphic
Damage irreversibilty

ABSTRACT

This study addresses ductile fracture of single grains in metals by modeling of the formation and propagation of transgranular cracks. A proposed model integrates gradient-extended hardening, phase-field modeling for fracture, and crystal plasticity. It is presented in a thermodynamical framework in large deformation kinematics and accounts for damage irreversibility. A micromorphic approach for variationally and thermodynamically consistent damage irreversibility is adopted. The main objective of this work is to analyze the capability of the proposed model to describe transgranular crack propagation. Further, the micromorphic approach for damage irreversibility is evaluated in the context of the presented ductile phase-field model. This is done by analyzing the impact of gradient-enhanced hardening considering micro-free and micro-hard boundary conditions, studying the effect of the micromorphic regularization parameter, evaluating the performance of the model in ratcheting loading and testing its capability to predict three-dimensional crack propagation. In order to solve the fully coupled global and local equation systems, a staggered solution scheme that extends to the local level is presented.

1. Introduction

The initiation and propagation of cracks, which play an important role in determining the lifespan of engineering components, are preceded by significant plastic deformation. To simulate and predict the fracture process, particularly the initiation and growth of short (microscopic) cracks evolving into macroscopic cracks, it is imperative to delve into detailed modeling at the grain scale.

Damage and fracture within the grains may occur in the slip planes as a consequence of the localization of plastic slip. The propagation of small cracks follows crystallographic directions (Rovinelli et al., 2018), making it natural to couple damage modeling with crystal plasticity (cf. Flouriot et al., 2003; Aslan et al., 2011). In order to capture size-dependent behavior resulting from geometrical necessary dislocations at grain boundaries (or other obstacles), gradient-extended crystal plasticity models have been introduced, see e.g. Gurtin (2002), Evers et al. (2004) and Ekh et al. (2007). These models introduce a length-scale parameter, providing a size-dependent response and helping to overcome mesh-dependence issues for softening behavior (De Borst et al., 1999).

For modeling the fracture of grains, a combination of damage mechanics and crystal plasticity has been extensively employed, as for example seen in Aslan et al. (2011) and Ekh et al. (2004). The phase-field approach has in recent years become a popular choice for modeling fracture. In this approach, the discrete crack is represented as a diffuse field whose width is determined by a length scale parameter. The advantageous feature of phase-field modeling in fracture lies in its capability to predict arbitrary crack propagation patterns, including crack branching and coalescence. Moreover, in elasticity, it aligns with classical fracture mechanics, when the length scale parameter approaches zero. This modeling approach has found application in predicting ductile fracture in several works, as discussed in Alessi et al. (2018) and references therein, and has been coupled with crystal plasticity in Hernandez Padilla and Markert (2014), De Lorenzis et al. (2016) and Maloth and Ghosh (2023). It has been shown to be a promising approach for transgranular fracture of metals.

Phase-field models, however, require special treatment in order to ensure damage irreversibility, which is necessary to obtain physically realistic responses upon unloading and reversed loading. While a number of different approaches have been suggested to address its numerical treatment, e.g. Bourdin et al. (2008), Miehe et al. (2010b), Gerasimov and De Lorenzis (2019) and Alessi et al. (2015), one of the most commonly adopted approaches is the so called history-variable approach by Miehe et al. (2010a). This approach introduces the history variable in the strong form of the phase-field equation. It thereby renders it impossible to retrieve the energy functional back from the strong

* Corresponding author.
E-mail address: kim.auth@chalmers.se (K.L. Auth).

https://doi.org/10.1016/j.euromechsol.2024.105418
Received 26 February 2024; Received in revised form 28 June 2024; Accepted 10 August 2024
Available online 12 August 2024

from and thus results in the loss of variational consistency. Bharali et al. (2023) have recently proposed to use a micromorphic approach instead, offering the advantage that irreversibility can be directly formulated on a local damage field. The micromorphic extension, as presented in Forest (2009), has in earlier works addressed challenges such as avoiding mesh dependence for softening behavior (Dimitrijevic and Hackl, 2011), modeling size-dependent hardening (Dimitrijevic and Hackl, 2011), and enhancing numerical robustness (Miehe et al., 2017).

The objective of this work is to propose a ductile fracture model that allows to account for micro-structural effects on crack initiation and growth in metals. We aim at integrating gradient-extended hardening and phase-field modeling within a crystal plasticity framework. Since ductile fracture in metals is usually preceeded by the development of large amounts of (plastic) strain, the model is presented in a thermodynamical framework with large deformation kinematics. The incorporation of gradient-extended hardening is motivated by the resistance to edge dislocation motion at grain boundaries which affects the stress field and therefore the fracture behavior.

The novelty of the presented work lies in the incorporation of the gradient-hardening extension to a crystal plasticity based phase field fracture model on one hand and in the choice of damage irreversibility criterion on the other hand. Bharali et al. (2023) have applied the micromorphic irreversibility criterion to a small strain elasticity framework with a porous media extension and employed a convexification scheme in order to solve the resulting equation system monolitically. Additionally to applying the irreversibility scheme to a more complex finite strain base model, we employ a staggered solution scheme without convexification. Primary objectives of the paper are to analyze model behavior for different choices of gradient hardening boundary conditions, as well as the interaction between the micromorphic and ductile contributions to the phase-field formulation. We further explore the robustness of the micromorphic phase-field formulation to the change of global solution strategy and the related removal of the convexification technique.

The structure of the paper is as follows: Section 2 provides an overview of the thermodynamic framework underlying the model. Section 3 introduces a prototype large strain crystal plasticity model, while Section 4 deals with formulations concerning damage irreversibility. The weak formulation of the balance equations is outlined in Section 5. Section 6 comments on important details of the numerical implementation, in particular on the staggered solution scheme in presence of multiple local variables. To highlight aspects of the proposed model, numerical results for single crystal boundary value problems in two-dimensional (2D) and three-dimensional (3D) settings are presented and analyzed in Section 7. Concluding remarks are given in Section 8.

2. Thermodynamic modeling framework

In this section, a thermodynamic framework for a phase-field fracture model based on an underlying gradient crystal plasticity formulation is presented. The derivations follow Ekh et al. (2007) for a gradient crystal plasticity model but are here extended with phase-field fracture. For comparison, a derivation based on the microforce balances is given in Appendix B.

We formulate the model in a large strain setting and assume a multiplicative decomposition of the deformation gradient $\boldsymbol{F}$ into an elastic part $\boldsymbol{F}_\mathrm{e}$ and a plastic part $\boldsymbol{F}_\mathrm{p}$

$$\boldsymbol{F} = \boldsymbol{F}_\mathrm{e} \cdot \boldsymbol{F}_\mathrm{p} \,. \tag{1}$$

Further, we introduce the set of isotropic hardening variables $\{k_\alpha\}_{\alpha=1}^{n_\alpha}$, where k_α signifies the isotropic hardening variable on the α-th of n_α slip systems and a damage (phase-field) variable d. The free energy Ψ is then assumed to depend on the elastic Cauchy–Green deformation gradient $\boldsymbol{C}_\mathrm{e} = \boldsymbol{F}_\mathrm{e}^\mathrm{T} \cdot \boldsymbol{F}_\mathrm{e}$, the state variable q, the isotropic hardening variables $\{k_\alpha\}_{\alpha=1}^{n_\alpha}$, the damage variable d and the spatial gradients $\{\boldsymbol{\nabla}_0 k_\alpha\}_{\alpha=1}^{n_\alpha}$ and $\boldsymbol{\nabla}_0 d$

$$\Psi = \Psi\left(\boldsymbol{C}_\mathrm{e},\, q,\, \{k_\alpha\}_{\alpha=1}^{n_\alpha},\, \{\boldsymbol{\nabla}_0 k_\alpha\}_{\alpha=1}^{n_\alpha},\, d,\, \boldsymbol{\nabla}_0 d\right) \tag{2}$$

The dissipation inequality under quasistatic and isothermal conditions is given by

$$\int_{V_0} \boldsymbol{P} : \dot{\boldsymbol{F}}\, \mathrm{d}V_0 - \int_{V_0} \dot{\Psi}\, \mathrm{d}V_0 \geq 0 \,. \tag{3}$$

where $\boldsymbol{P}$ is the first Piola–Kirchhoff stress, $\boldsymbol{F}$ is the deformation gradient and V_0 represents the initial domain with boundary Γ_0. Introducing the free energy (2) into the dissipation inequality (3) and using the standard Coleman–Noll arguments (Coleman and Noll, 1963) yields the elastic second Piola–Kirchhoff stress $\boldsymbol{S}_\mathrm{e}$ as (see e.g. Simo (1988))

$$\boldsymbol{S}_\mathrm{e} = 2\,\frac{\partial \Psi}{\partial \boldsymbol{C}_\mathrm{e}} \,, \tag{4}$$

and we obtain the reduced dissipation inequality

$$\mathcal{D} = \int_{V_0} \left(\boldsymbol{M}_\mathrm{e} : \boldsymbol{L}_\mathrm{p} - \frac{\partial \Psi}{\partial q}\,\dot{q} - \sum_{\alpha=1}^{n_\alpha} \frac{\partial \Psi}{\partial k_\alpha}\,\dot{k}_\alpha - \sum_{\alpha=1}^{n_\alpha} \frac{\partial \Psi}{\partial \boldsymbol{\nabla}_0 k_\alpha} \cdot \boldsymbol{\nabla}_0 \dot{k}_\alpha \right.$$
$$\left. - \frac{\partial \Psi}{\partial d}\,\dot{d} - \frac{\partial \Psi}{\partial \boldsymbol{\nabla}_0 d} \cdot \boldsymbol{\nabla}_0 \dot{d} \right) \mathrm{d}V_0 \geq 0 \,. \tag{5}$$

In Eqs. (4)–(5), the Mandel stress $\boldsymbol{M}_\mathrm{e} = \boldsymbol{C}_\mathrm{e} \cdot \boldsymbol{S}_\mathrm{e}$, like the second Piola–Kirchhoff stress on the intermediate configuration, as well as the plastic velocity gradient $\boldsymbol{L}_\mathrm{p} = \dot{\boldsymbol{F}}_\mathrm{p} \cdot \boldsymbol{F}_\mathrm{p}^{-1}$ were introduced. Using the divergence theorem, the reduced dissipation inequality can be rewritten as

$$\mathcal{D} = \int_{V_0} \left(\boldsymbol{M}_\mathrm{e} : \boldsymbol{L}_\mathrm{p} + Q\,\dot{q} + \sum_{\alpha=1}^{n_\alpha} \kappa_\alpha\,\dot{k}_\alpha + Y\,\dot{d} \right) \mathrm{d}V_0$$
$$+ \int_{\partial V_0} \left(\sum_{\alpha=1}^{n_\alpha} \kappa_\alpha^\Gamma\,\dot{k}_\alpha + Y^\Gamma\,\dot{d} \right) \mathrm{d}A_0 \geq 0 \,, \tag{6}$$

where $Q = -\partial\Psi/\partial q$ and the gradient-extended dissipative hardening stress κ_α and its boundary "traction" κ_α^Γ were introduced as

$$\kappa_\alpha = -\frac{\partial \Psi}{\partial k_\alpha} + \boldsymbol{\nabla}_0 \cdot \frac{\partial \Psi}{\partial \boldsymbol{\nabla}_0 k_\alpha} \,, \tag{7}$$

$$\kappa_\alpha^\Gamma = -\boldsymbol{N} \cdot \frac{\partial \Psi}{\partial \boldsymbol{\nabla}_0 k_\alpha} \,, \tag{8}$$

where $\boldsymbol{N}$ is the unit normal to Γ_0. The corresponding dissipative quantities for the phase-field are

$$Y = -\frac{\partial \Psi}{\partial d} + \boldsymbol{\nabla}_0 \cdot \frac{\partial \Psi}{\partial \boldsymbol{\nabla}_0 d} \tag{9}$$

$$Y^\Gamma = -\boldsymbol{N} \cdot \frac{\partial \Psi}{\partial \boldsymbol{\nabla}_0 d} \tag{10}$$

The phase-field equation is obtained by assuming that $Y = 0$ (purely energetic)

$$-\frac{\partial \Psi}{\partial d} + \boldsymbol{\nabla}_0 \cdot \frac{\partial \Psi}{\partial \boldsymbol{\nabla}_0 d} = 0 \tag{11}$$

and thereby it can be noted that the phase-field will not contribute to the dissipation on V_0. Hence, the reduced dissipation inequality becomes

$$\mathcal{D} = \int_{V_0} \left(\boldsymbol{M}_\mathrm{e} : \boldsymbol{L}_\mathrm{p} + Q\,\dot{q} + \sum_{\alpha=1}^{n_\alpha} \kappa_\alpha\,\dot{k}_\alpha \right) \mathrm{d}V_0$$
$$+ \int_{\partial V_0} \left(\sum_{\alpha=1}^{n_\alpha} \kappa_\alpha^\Gamma\,\dot{k}_\alpha + Y^\Gamma\,\dot{d} \right) \mathrm{d}A_0 \geq 0 \tag{12}$$

Appendix B presents an alternative derivation in terms of microforce balances. Opposed to the derivation in Appendix B, we do not obtain a local definition of the dissipation inequality in Eq. (12), instead we obtain boundary terms, which is not obtained from the microforce balance based derivation.

These boundary terms must be respected when formulating boundary conditions for the field equations. The resulting field Eqs. (7) and (11) are the same independently which derivation approach is chosen.

3. Prototype crystal plasticity model

We will assume the following form of the free energy

$$\Psi = g_e\left(d,\epsilon^p\right)\hat{\Psi}_e\left(\boldsymbol{C}_e\right) + g_p\left(d\right)\hat{\Psi}_p\left(\{k_\alpha\}_{\alpha=1}^{n_\alpha},\{\boldsymbol{\nabla}_0 k_\alpha\}_{\alpha=1}^{n_\alpha}\right) + \Psi_d\left(d,\boldsymbol{\nabla}_0 d\right) \tag{13}$$

The effective (undamaged) elastic part of the free energy $\hat{\Psi}_e$ is assumed to be of Neo-Hookean type

$$\hat{\Psi}_e\left(\boldsymbol{C}_e\right) = \frac{\mu}{2}\left(\mathrm{tr}(\boldsymbol{C}_e)-3\right) - \mu\,\ln(J_e) + \frac{\lambda}{2}\left(\ln(J_e)\right)^2 \quad \text{with } J_e^2 = \det(\boldsymbol{C}_e) \tag{14}$$

where λ and μ are the elastic Lamé constants. For simplicity, we have assumed elastic isotropy and disregarded a tension–compression split. The elastic degradation function g_e is adopted from the ductile fracture model presented by Ambati et al. (2015)

$$g_e\left(d,\epsilon^p\right) = (1-d)^{2\left(\epsilon^p/\epsilon^p_{\mathrm{crit}}\right)^n}, \tag{15}$$

where ϵ^p is the accumulated plastic strain (in the thermodynamic modeling framework above represented by q). It can be noted that the degradation is only active when $\epsilon_p > 0$ and that the parameters $\epsilon^p_{\mathrm{crit}}$ and $n > 0$ control how the degradation increases when ϵ^p increases. As shown by Ambati et al. (2015), the formulation gives a positive contribution to the dissipation, i.e. $Q\,\dot{q} \geq 0$.

The effective plastic free energy $\hat{\Psi}_p$ is chosen as (compare Ekh et al. (2007))

$$\hat{\Psi}_p = \frac{1}{2}\sum_{\alpha=1}^{n_\alpha} H_\alpha\, k_\alpha^2 + \frac{l_g^2}{2}\sum_{\alpha=1}^{n_\alpha} H_\alpha^g\,(\bar{\boldsymbol{s}}_\alpha\cdot\boldsymbol{\nabla}_0 k_\alpha)^2, \tag{16}$$

where H_α is the isotropic hardening modulus, H_α^g is the gradient-enhanced hardening modulus and l^g is the length scale for gradient-enhanced hardening. We adopt the standard assumption that the slip direction $\bar{\boldsymbol{s}}_\alpha$ and normal vector to the slip plane $\bar{\boldsymbol{m}}_\alpha$ on the intermediate configuration are fixed (and equal to their corresponding vectors on the undeformed configuration). For simplicity, the plastic degradation function is chosen as $g_p = 1$. The yield function Φ_α is defined in terms of the effective Schmid stress $\hat{\tau}_\alpha$ as

$$\Phi_\alpha = \left|\hat{\tau}_\alpha\right| - (\tau_y + \kappa_\alpha) \tag{17}$$

with $\hat{\tau}_\alpha = \tau_\alpha / g_e(d,\epsilon^p)$ wherein τ_α is the standard crystal plasticity Schmid stress $\tau_\alpha = \boldsymbol{M}_e : \left(\bar{\boldsymbol{s}}_\alpha\otimes\bar{\boldsymbol{m}}_\alpha\right)$. Furthermore, τ_y is the initial yield stress. The evolution equation for the plastic velocity gradient is assumed to be of associative type

$$\bar{\boldsymbol{L}}_p = \dot{\boldsymbol{F}}_p\cdot\boldsymbol{F}_p^{-1} = \sum_{\alpha=1}^{n_\alpha}\dot{\lambda}_\alpha\frac{\partial\Phi_\alpha}{\partial\boldsymbol{M}_e} = \sum_{\alpha=1}^{n_\alpha}\frac{\dot{\lambda}_\alpha}{g_e(d,\epsilon^p)}\left(\bar{\boldsymbol{s}}_\alpha\otimes\bar{\boldsymbol{m}}_\alpha\right)\,\mathrm{sign}\left(\hat{\tau}_\alpha\right) \tag{18}$$

and we apply a viscoplastic regularization for the multiplier

$$\dot{\lambda}_\alpha = \frac{1}{t^*}\left\langle\frac{\Phi_\alpha}{\sigma_d}\right\rangle^m, \tag{19}$$

where t^*, m and σ_d control the viscosity of the model and $\langle\bullet\rangle$ denotes Macualey brackets. The accumulated plastic strain ϵ^p is based on $\dot{\lambda}_\alpha$ defined as

$$\epsilon_p = \int_0^t\sqrt{\sum_{\alpha=1}^{n_\alpha}\dot{\lambda}_\alpha^2}\,\mathrm{d}t. \tag{20}$$

The gradient-extended hardening stress κ_α is derived from Eq. (7) as

$$\kappa_\alpha = -H_\alpha\,k_\alpha + H_\alpha^g\,l_g^2\,\bar{\boldsymbol{s}}_\alpha\cdot(\boldsymbol{\nabla}_0\otimes\boldsymbol{\nabla}_0 k_\alpha)\cdot\bar{\boldsymbol{s}}_\alpha \tag{21}$$

and the evolution of the hardening variable k_α is also assumed to be of associative type

$$\dot{k}_\alpha = \dot{\lambda}_\alpha\frac{\partial\Phi_\alpha}{\partial\kappa_\alpha} = -\dot{\lambda}_\alpha. \tag{22}$$

These assumptions for the hardening can be extended, see e.g. Bargmann et al. (2010) to account for more complex models such as kinematic hardening, cross-hardening and nonlinear hardening.

For the phase-field fracture model, the free energy contribution is based on an AT2 surface energy functional Γ_d, cf. Ambrosio and Tortorelli (1990)

$$\Psi_d\left(d,\boldsymbol{\nabla}_0 d\right) = \mathcal{G}_0^d\,\Gamma_d\left(d,\boldsymbol{\nabla}_0 d\right) \quad \text{with } \Gamma_d = \frac{1}{2\ell_0}\left(d^2 + \ell_0^2\left|\boldsymbol{\nabla}_0 d\right|^2\right) \tag{23}$$

where $\mathcal{G}_0^d$ represents fracture toughness and ℓ_0 is the length-scale parameter controlling the width of the diffuse crack model. By inserting the choices of degradation functions and Ψ_d, the phase-field Eq. (11) becomes

$$2\left(\epsilon^p/\epsilon^p_{\mathrm{crit}}\right)^n(1-d)^{2\left(\epsilon^p/\epsilon^p_{\mathrm{crit}}\right)^n-1}\hat{\Psi}_e - \frac{\mathcal{G}_0^d}{\ell_0}d + \mathcal{G}_0^d\,\ell_0\,\boldsymbol{\nabla}_0\cdot\boldsymbol{\nabla}_0 d = 0 \tag{24}$$

which is similar to the formulation used in De Lorenzis et al. (2016) but extended with the exponent n.

4. Irreversibility

As discussed in the introduction, one of the most common approaches for enforcing damage irreversibility is the history variable approach introduced by Miehe et al. (2010a) where the effective elastic free energy $\hat{\Psi}_e$ in the phase-field equation (Eq. (24)) is replaced by a history variable

$$\mathcal{H}(t) = \max_{\tilde{t}\leq t}\hat{\Psi}_e. \tag{25}$$

This approach though has been shown to be variationally inconsistent, see e.g. De Lorenzis and Gerasimov (2020). Within this work we therefore explore a micromorphic approach (Forest, 2009), which has recently been shown to allow for a variationally consistent framework for locally enforced damage irreversibility (Bharali et al., 2023).

It introduces an additional local variable φ and includes a penalty term in the free energy that connects the global damage d with the (new) local damage φ. The local damage φ then replaces d in all terms except for the new penalty term and the damage gradient term.

$$\begin{aligned}\Psi = {} & g_e\left(\varphi,\epsilon^p\right)\hat{\Psi}_e\left(\boldsymbol{C}_e\right) + g_p\left(\varphi\right)\hat{\Psi}_p\left(\{k_\alpha\}_{\alpha=1}^{n_\alpha},\{\boldsymbol{\nabla}_0 k_\alpha\}_{\alpha=1}^{n_\alpha}\right)\\ & + \Psi_d\left(\varphi,\boldsymbol{\nabla}_0 d\right) + \frac{\alpha}{2}(\varphi-d)^2\end{aligned} \tag{26}$$

The dissipation inequality (6) is thereby modified to

$$\begin{aligned}\mathcal{D} = {} & \int_{V_0}\left(\boldsymbol{M}_e : \boldsymbol{L}_p + Q\,\dot{q} + \sum_{\alpha=1}^{n_\alpha}\kappa_\alpha\,\dot{k}_\alpha + Y_\varphi\,\dot{\varphi} + Y_d\,\dot{d}\right)\mathrm{d}V_0\\ & + \int_{\partial V_0}\left(\sum_{\alpha=1}^{n_\alpha}\kappa_\alpha^\Gamma\,\dot{k}_\alpha + Y^\Gamma\,\dot{d}\right)\mathrm{d}A_0 \geq 0\end{aligned} \tag{27}$$

where equivalently to the procedure leading to Eq. (11), $Y_d = 0$ yields the global phase-field equation

$$Y_d = \alpha(\varphi-d) + \mathcal{G}_0^d\,\ell_0\,\boldsymbol{\nabla}_0\cdot\boldsymbol{\nabla}_0 d = 0 \tag{28}$$

and hence the global phase-field d does not contribute to the dissipation on V_0. The micromorphic approach introduces an additional regularization to the model. In Miehe et al. (2017) it was mainly used for robustness of numerical implementation but can as suggested by Bharali et al. (2023) conveniently be used to ensure irreversibility. The evolution of the local phase-field φ is then derived from the inequality $Y_\varphi\,\dot{\varphi} \geq 0$. For the suggested choice of model Y_φ is given by

$$Y_\varphi = -\frac{\partial\Psi}{\partial\varphi} = 2\left(\epsilon^p/\epsilon^p_{\mathrm{crit}}\right)^n(1-\varphi)^{2\left(\epsilon^p/\epsilon^p_{\mathrm{crit}}\right)^n-1}\hat{\Psi}_e - \frac{\mathcal{G}_0^d}{\ell_0}\varphi - \alpha(\varphi-d). \tag{29}$$

For pure loading, the local phase-field φ can be computed from assuming that Y_φ is energetic, i.e. $Y_\varphi = 0$. In order to obtain a thermodynamically consistent formulation for unloading however, the full inequality must be considered. By introducing an intermediate local

variable $\tilde{\varphi} = \arg\{Y_\varphi(\varphi) = 0\}$, the Karush-Kuhn-Tucker conditions to ensure irreversibility of φ can be formulated as

$$\dot{\varphi} \geq 0\,, \quad \dot{\varphi}\, f_\varphi = 0\,, \quad f_\varphi = \tilde{\varphi} - \varphi \leq 0\,. \tag{30}$$

Thereby, we obtain $Y_\varphi\, \dot{\varphi} = 0$, since $Y_\varphi = 0$ during loading ($\varphi = \tilde{\varphi}$) and $\dot{\varphi} = 0$ during unloading ($\varphi = \text{const}$). Notice that the local phase-field here becomes a history variable.

5. Weak form of balance equations

The weak form of balance of momentum when neglecting inertial forces and body forces is expressed in terms of the first Piola–Kirchhoff stress $\boldsymbol{P}$ as

$$\delta\mathcal{W}^{\mathrm{u}} = \int_{V_0} \boldsymbol{P} : \left(\delta\boldsymbol{u} \otimes \boldsymbol{\nabla}_0\right) \mathrm{d}V_0 - \int_{\partial V_0} \boldsymbol{t}_0^* \cdot \delta\boldsymbol{u}\, \mathrm{d}A_0\,, \tag{31}$$

where $\boldsymbol{t}_0^*$ is a prescribed traction on the boundary ∂V_0. The expression for the gradient-extended hardening stress κ_α in Eq. (21) is, due to the spatial gradients, also a field equation. We adopt the dual mixed procedure described in Svedberg and Runesson (1998) and introduce

$$\boldsymbol{g}_\alpha = \boldsymbol{\nabla}_0 k_\alpha \tag{32}$$

whereby

$$\kappa_\alpha = -H_\alpha\, k_\alpha + H_\alpha^{\mathrm{g}}\, l_{\mathrm{g}}^2\, \bar{\boldsymbol{s}}_\alpha \cdot \boldsymbol{\nabla}_0 \boldsymbol{g}_\alpha \cdot \bar{\boldsymbol{s}}_\alpha \tag{33}$$

becomes a local equation. Instead, the weak form of Eq. (32) is introduced as a field equation and by using the divergence theorem we obtain

$$\delta\mathcal{W}_\alpha^{\mathrm{g}} = \int_{V_0} \boldsymbol{g}_\alpha\, \delta\boldsymbol{g}_\alpha\, \mathrm{d}V_0 - \int_{\partial V_0} k_\alpha\, \boldsymbol{N} \cdot \delta\boldsymbol{g}_\alpha\, \mathrm{d}A_0 + \int_{V_0} k_\alpha\, \boldsymbol{\nabla}_0 \cdot \delta\boldsymbol{g}_\alpha\, \mathrm{d}V_0\,. \tag{34}$$

This procedure has been shown to be numerically robust (Ekh et al., 2007; Carlsson et al., 2017) and has the same benefit as a micromorphic approach that no special treatment to account for loading/unloading conditions is needed since it can be controlled locally in the material points. Finally, the phase-field Eq. (28) is formulated in weak form as

$$\begin{aligned}\delta\mathcal{W}^{\mathrm{d}} = &\int_{V_0} \alpha\,(\varphi - d)\; \delta d\, \mathrm{d}V_0 + \int_{\partial V_0} \mathcal{G}_0^{\mathrm{d}}\, \ell_0\, \boldsymbol{N} \cdot \boldsymbol{\nabla}_0 d\; \delta d\, \mathrm{d}A_0 \\ &- \int_{V_0} \mathcal{G}_0^{\mathrm{d}}\, \ell_0\, \boldsymbol{\nabla}_0 d \cdot \boldsymbol{\nabla}_0 \delta d\, \mathrm{d}V_0\,,\end{aligned} \tag{35}$$

where the standard boundary condition $\boldsymbol{N} \cdot \boldsymbol{\nabla}_0 d = 0$ will be assumed whereby the boundary integral term disappears.

The choice of the micromorphic penalty parameter α can conveniently be based on the employed effective fracture energy $\mathcal{G}_0^{\mathrm{d}}/\ell_0$ by defining it in terms of a dimensionless scalar β such that $\alpha = \beta\, \mathcal{G}_0^{\mathrm{d}}/\ell_0$.

6. Numerical implementation

6.1. Time integration

Time integration schemes are needed for the plastic evolution equations, Eqs. (18) and (22), as well as for the accumulated plastic strain, Eq. (20) and the evolution of the local phase-field, Eq. (30). Backward Euler time integration is applied to the evolution equations for the plastic deformation gradient $\boldsymbol{F}_{\mathrm{p}}$ and the hardening variables k_α. For time points ${}^{\mathrm{n+1}}t$ and ${}^{\mathrm{n}}t$, a time step $\Delta t = {}^{\mathrm{n+1}}t - {}^{\mathrm{n}}t$ and $\Delta\lambda_\alpha = \Delta t\, {}^{\mathrm{n+1}}\dot{\lambda}_\alpha$, we obtain the following expressions

$${}^{\mathrm{n+1}}k_\alpha = {}^{\mathrm{n}}k_\alpha - {}^{\mathrm{n+1}}\Delta\lambda_\alpha \tag{36}$$

$${}^{\mathrm{n+1}}\boldsymbol{F}_{\mathrm{p}}^{-1} = {}^{\mathrm{n}}\boldsymbol{F}_{\mathrm{p}}^{-1} \cdot \left(\boldsymbol{I} - \sum_{\alpha=1}^{n_\alpha} \frac{{}^{\mathrm{n+1}}\Delta\lambda_\alpha}{g_{\mathrm{e}}({}^{\mathrm{n+1}}\varphi)} \left(\bar{\boldsymbol{s}}_\alpha \otimes \bar{\boldsymbol{m}}_\alpha\right) \operatorname{sign}\left({}^{\mathrm{n+1}}\tau_\alpha\right)\right). \tag{37}$$

The signs of the Schmid stresses ${}^{\mathrm{n+1}}\tau_\alpha$ are computed based on the elastic trial stress. The evolution of the local phase-field φ is discretized as

$${}^{\mathrm{n+1}}\varphi = \max\left({}^{\mathrm{n+1}}\tilde{\varphi},\ {}^{\mathrm{n}}\varphi\right) \tag{38}$$

and thereby accounting for the irreversibility condition. An explicit scheme is applied to the accumulated plastic strain ϵ^{p}, such that the elastic degradation is computed based on the accumulated plastic strain from the previous time step ${}^{\mathrm{n}}\epsilon^{\mathrm{p}}$

$$g_{\mathrm{e}}(\varphi) = (1-\varphi)^{2\left({}^{\mathrm{n}}\epsilon^{\mathrm{p}}/\epsilon^{\mathrm{p}}_{\mathrm{crit}}\right)^n}\,. \tag{39}$$

Thereby, two coupled local residual equations with unknowns ${}^{\mathrm{n+1}}\tilde{\varphi}$ and ${}^{\mathrm{n+1}}\Delta\lambda_\alpha$ need to be solved for every time step within the global residual Eqs. (31), (34) and (35).

$$\mathcal{R}_{\Delta\lambda_\alpha}\left(\Delta\lambda_\alpha,\, \varphi\right) = \Delta\lambda_\alpha - \frac{\Delta t}{t^*} \left\langle \frac{\boldsymbol{\Phi}_\alpha\left(\boldsymbol{C},\, \boldsymbol{\nabla}_0 \boldsymbol{g}_\alpha,\, \Delta\lambda_\alpha,\, \varphi\right)}{\sigma_{\mathrm{d}}} \right\rangle^{\mathrm{m}} \tag{40}$$

$$\mathcal{R}_\varphi\left(\Delta\lambda_\alpha,\, \tilde{\varphi}\right) = -\frac{\partial g_{\mathrm{e}}(\tilde{\varphi})}{\partial\tilde{\varphi}} \hat{\Psi}_{\mathrm{e}}\left(\boldsymbol{C},\, \Delta\lambda_\alpha,\, \tilde{\varphi}\right) - \frac{\mathcal{G}_0^{\mathrm{d}}}{\ell_0}\, \tilde{\varphi} - \alpha\,(\tilde{\varphi} - d) \tag{41}$$

6.2. Dimension-free formulation

For the following presentation of numerical results a representation with dimension free volumes and derivatives is employed. We introduce a global length scale L representing the overall domain size and dimension free coordinates $\boldsymbol{\xi}$ such that the initial coordinates $\boldsymbol{X}$ can be expressed as

$$\boldsymbol{X} = \boldsymbol{\xi}\, L \tag{42}$$

which also leads to the following relations

$$\boldsymbol{\nabla}_0 = \boldsymbol{\nabla}_\xi\, \frac{1}{L}\,, \quad V_0 = V_\xi\, L^3\,, \quad A_0 = A_\xi\, L^2\,. \tag{43}$$

The field variables $\boldsymbol{u}$ and $\boldsymbol{g}_\alpha$ can be expressed by their dimensionless counterparts $\boldsymbol{u}_\xi$ and $\boldsymbol{g}_{\alpha\xi}$

$$\boldsymbol{u} = \boldsymbol{u}_\xi\, L\,, \quad \boldsymbol{g} = \frac{1}{L}\, \boldsymbol{g}_{\alpha\xi}\,. \tag{44}$$

Further, we introduce the dimension-free phase-field length-scale ℓ_ξ, the dimension-free gradient hardening length-scale l_ξ^{g} and the effective fracture energy $\mathcal{G}_\xi^{\mathrm{d}}$ as

$$\ell_\xi = \frac{\ell_0}{L}\,, \quad l_\xi^{\mathrm{g}} = \frac{l_{\mathrm{g}}}{L} \quad \text{and} \quad \mathcal{G}_\xi^{\mathrm{d}} = \frac{\mathcal{G}_0^{\mathrm{d}}}{L} \tag{45}$$

The weak forms, Eqs. (31), (34) and (35), can be formulated in terms of the dimension free coordinates as

$$\delta\mathcal{W}^{\mathrm{u}} = L^3 \left(\int_{V_\xi} \boldsymbol{P} : \left(\delta\boldsymbol{u}_\xi \otimes \boldsymbol{\nabla}_\xi\right) \mathrm{d}V_\xi - \int_{\partial V_\xi} \boldsymbol{t}_0^* \cdot \delta\boldsymbol{u}_\xi\, \mathrm{d}A_\xi\right), \tag{46}$$

$$\begin{aligned}\delta\mathcal{W}^{g} = L \Bigg(&\int_{V_\xi} \boldsymbol{g}_{\alpha\xi}\, \delta\boldsymbol{g}_{\alpha\xi}\, \mathrm{d}V_\xi - \int_{\partial V_\xi} k_\alpha\, \boldsymbol{N} \cdot \delta\boldsymbol{g}_{\alpha\xi}\, \mathrm{d}A_\xi \\ &+ \int_{V_\xi} k_\alpha\, \boldsymbol{\nabla}_\xi \cdot \delta\boldsymbol{g}_{\alpha\xi}\, \mathrm{d}V_\xi\Bigg),\end{aligned} \tag{47}$$

$$\begin{aligned}\delta\mathcal{W}^{\mathrm{d}} = L^3 \Bigg(&\int_{V_\xi} \beta\, \frac{\mathcal{G}_0^{\mathrm{d}}}{\ell_\xi}\,(\varphi - d)\; \delta d\, \mathrm{d}V_\xi + \int_{\partial V_\xi} \mathcal{G}_\xi^{\mathrm{d}}\, \ell_\xi\, \left(\boldsymbol{N} \cdot \boldsymbol{\nabla}_\xi d\right) \delta d\, \mathrm{d}A_\xi \\ &- \int_{V_\xi} \mathcal{G}_\xi^{\mathrm{d}}\, \ell_\xi\, \left(\boldsymbol{\nabla}_\xi d \cdot \boldsymbol{\nabla}_\xi \delta d\right) \mathrm{d}V_\xi\Bigg),\end{aligned} \tag{48}$$

showing that the solutions to the field equations are qualitatively independent of the global length scale L and quantitatively scale by L as introduced in Eqs. (42)–(45). The local equations including length-scale related parameters, Eqs. (21) and (29) can entirely be expressed in terms of the dimension-free parameters instead and are thereby not dependent on the choice of global length scale

$$\kappa_\alpha = -H_\alpha\, k_\alpha + H_\alpha^{\mathrm{g}}\, l_\xi^{\mathrm{g}2}\, \bar{\boldsymbol{s}}_\alpha \cdot \left(\boldsymbol{\nabla}_\xi \otimes \boldsymbol{\nabla}_\xi k_\alpha\right) \cdot \bar{\boldsymbol{s}}_\alpha\,, \tag{49}$$

$$Y_\varphi = 2\, \left(\epsilon^{\mathrm{p}}/\epsilon^{\mathrm{p}}_{\mathrm{crit}}\right)^n\, (1-\varphi)^{2\left(\epsilon^{\mathrm{p}}/\epsilon^{\mathrm{p}}_{\mathrm{crit}}\right)^n - 1} \hat{\Psi}_{\mathrm{e}} - \mathcal{G}_\xi^{\mathrm{d}}\, \varphi - \alpha\,(\varphi - d)\,. \tag{50}$$

Table 1
Field-wise tolerances applied for global convergence examination. A field is considered converged when either of the residual or the field tolerance (relating to the update of field variables during a single Newton-correction) is fulfilled.

	Global residual equation	Residual tolerance	Field tolerance
Displacement field $\boldsymbol{u}$	$\mathcal{R}^{\mathrm{u}}$, Eq. (31)	$L^2 \cdot 10^{-7}\,\mathrm{N\ mm^{-2}}$	$L \cdot 10^{-8}$
Hardening strain gradient $\boldsymbol{g}_\alpha$	$\mathcal{R}^{\mathrm{g}}$, Eq. (34)	$L^2 \cdot 10^{-11}$	$L^{-1} \cdot 10^{-6}$
Global phase-field d	$\mathcal{R}^{\mathrm{d}}$, Eq. (35)	$L^3 \cdot 10^{-10}\,\mathrm{N\ mm^{-3}}$	10^{-8}

6.3. Staggered solution scheme

We apply a staggered algorithm in order to solve the coupled problem. The algorithm is schematically represented in Fig. 1. The residual equations resulting from the weak forms, Eqs. (31), (34), and (35), are denominated $\mathcal{R}^{\mathrm{u}}$, $\mathcal{R}^{\mathrm{g}}$ and $\mathcal{R}^{\mathrm{d}}$. The equilibrium equation $\mathcal{R}^{\mathrm{u}}$ and the gradient-extended hardening field equation $\mathcal{R}^{\mathrm{g}}$ are solved in a monolithic way (referred to as $\mathcal{R}^{\mathrm{ug}}$ in Fig. 1) in the first staggered step and the global phase-field equation $\mathcal{R}^{\mathrm{d}}$ is solved in a second staggered step. Extending the staggered approach to the local equations, we group variables in two sets corresponding to the staggered steps: Set 1: $\{\boldsymbol{u}, \boldsymbol{g}_\alpha, k_\alpha, \boldsymbol{F}_{\mathrm{p}}\}$ and set 2: $\{d, \varphi\}$. Within each staggered iteration only the corresponding set of variables is updated, while the other set is frozen. Thus, a decoupling of the local equations is achieved and only one of the local residual equations needs to be solved within each staggered step. This is a similar staggered approach as the one taken by Ambati et al. (2015).

The local equations are solved by Newton iterations up to a tolerance of 10^{-8}. Field-wise convergence criteria on the global fields and their respective residuals are applied on the global system. A field is considered converged when either the norm of the residuals is below the respective residual tolerance or the norm of the update of field values in a Newton iteration is below the respective field tolerance. The tolerances applied for the numerical examples are displayed in Table 1.

The proposed model and finite element framework are implemented in the `Julia` programming language (Bezanson et al., 2017), making use of the `Ferrite.jl` (Carlsson et al., 2021) finite element and `Tensors.jl` (Carlsson and Ekre, 2019) tensor calculus toolboxes. Plots are generated using the data visualization system `Makie.jl` (Danisch and Krumbiegel, 2021).

7. Numerical experiments on single crystals

In this section, the behavior of the proposed prototype model is investigated. We first demonstrate that the presented model can reproduce well known behavior of crystal plasticity phase-field models from the literature. Then we display the effect of added gradient-enhanced hardening. Subsequently, it is demonstrated that the model is capable of capturing irreversible unloading. Finally, an example of damage development in a three-dimensional setting with inhomogeneities is shown.

The numerical examples, inspired by De Lorenzis et al. (2016), employ an I-shaped specimen in 2D (plane strain) and 3D. A base set of material parameters is shown in Table 2, deviating material parameters are given in the descriptions of the respective numerical examples. Fig. 2 shows the geometry and meshes for the numerical examples. Both cases represent the same cross-sectional geometry and employ unstructured meshes with a background element size of $0.04\,L$. Mesh refinements are conducted at the sides and in the center of the web, where the specimen is expected to break. The refinements in the 2D-mesh consist of elements with an average size of $0.005\,L$, resulting in 9 738 nodes and 19 390 linear triangular elements in total. In the 3D-mesh, center and sides are meshed with elements of 0.01 L average size and two positions are additionally refined with elements of $0.005\,L$ on average for imposing initial material inhomogeneities. The 3D mesh consists of 21 326 nodes and 123 183 linear tetrahedral elements in total. Linear function approximations have been used for all field variables. In all cases, FCC slip systems whose unit cell is aligned with the coordinate axes are used. The slip systems are shown in Table 3 in Appendix A. The slip systems with slip directions perpendicular to the loading direction are omitted in all examples, since they have a negligible impact on the plastification. Sections 7.1 and 7.2 thereby use 8 slip systems each. Sections 7.3 and 7.4 only employ the four most active slip systems, that is slip systems 1, 4, 7 and 10. Notice that the system size of the $\mathcal{R}^{\mathrm{ug}}$-equation system grows quickly with the number of slip systems since it requires a vector field for the displacement field $\boldsymbol{u}$ and a vector field per slip system for the gradient fields $\boldsymbol{g}_\alpha$. This also means that the mesh size at which the major computational cost shifts from being associated with solving the local problems to being associated with the global linear solver is much smaller than for comparable systems without gradient-extension.

The reduction of the number of slip systems is motivated by the reduction of the numerical cost. The number of employed slip systems represents a compromise between the computational cost of the respective simulations and the accuracy of the obtained plastification. When choosing the required number of slip systems, it should be noticed that the active slip systems might vary due to large deformations and especially during the final stage of the fracturing process.

The I-shaped specimen is clamped on the bottom side and loaded by prescribing a displacement of $0.1\,L\,/\,t^*$ in the vertical direction on the upper side, while the horizontal displacement is zero.

7.1. Boundary conditions for gradient-enhanced hardening

In a first step, we consider the I-shaped specimen under plane strain conditions. We investigate the model behavior without gradient hardening, $l^{\mathrm{g}} = 0.0\,L$, as well as for the two trivial possibilities of boundary conditions on the strain gradient fields: micro-hard, $k_\alpha = 0$, and micro-free, $\boldsymbol{g}_\alpha \cdot \bar{\boldsymbol{s}}_\alpha = 0$, slip transfer. Note that both boundary conditions give no dissipation on the boundary, $\kappa_\alpha^{\Gamma} k_\alpha = 0$ in Eq. (12). Fig. 3 displays the reaction force response of the three cases. All three scenarios first undergo a linear elastic loading phase, followed by hardening and finally softening behavior. The linear elastic behavior is obtained even though an AT2-type phase-field model is applied, since the material degradation is based on a combination of accumulated plastic strain and the phase-fields (compare Eq. (15)). As a consequence, the local phase-field can only develop once at least a small amount of plastic strain develops, thus recovering a true linear elastic phase. As expected, the gradient hardening together with micro-hard conditions gives a stiffer response in the nonlinear regime. Fig. 4 shows the material degradation at the last converged load step. The well known diamond shape crack pattern (compare e.g. De Lorenzis et al. (2016)) is recovered without gradient hardening. The behavior under micro-free boundary conditions is similar, but shows smoothing of the degradation field. Micro-hard boundary conditions disallow the development of plastic strains on the boundary in a weak sense (for the chosen algorithmic formulation). Consequently, no damage can develop on the boundaries for a sufficiently fine mesh. The micro-hard response is more sensitive to the mesh, which is shown in Fig. 4 by the fact that an unsymmetric mesh gives a slightly unsymmetric response. The mesh for the micro-hard case has however already been refined compared to the other cases by using elements with an average size of 0.25 mm on the left and right boundaries.

Notice that micro-free and micro-hard boundary conditions represent idealized conditions. Micro-hard boundary conditions represent boundaries that do not allow any slip transmission and thereby completely prevent plastic deformation on the boundary. Micro-free boundary conditions in contrast represent the case where a boundary does not possess any resistance against slip transmission. In the following simulations we choose to apply micro-free boundary conditions in order to represent free outer boundaries. In the case of polycrystalline

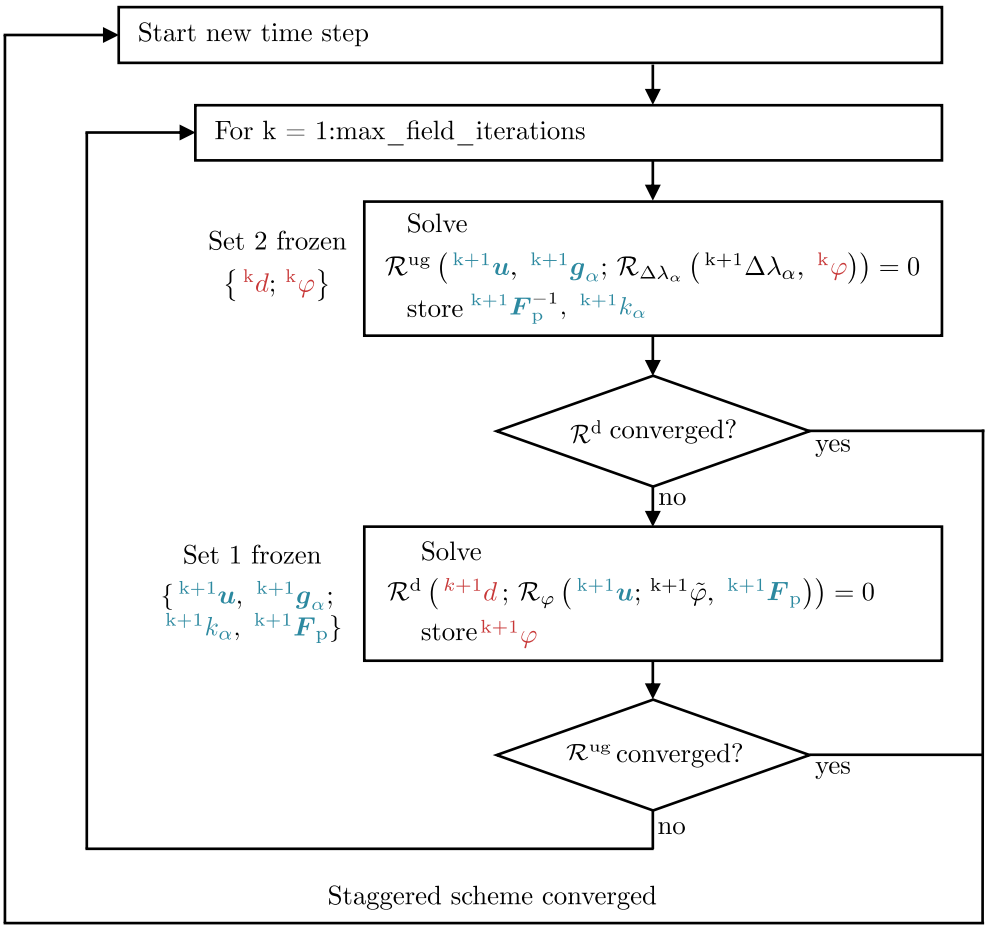

Fig. 1. Staggered iteration scheme for the global system solver. The global and local variables are grouped in two groups extending the staggered solution scheme to the local equation system. The staggered algorithm solves for one set of variables at a time while freezing the other set. The iteration between the sets is stopped once the global residuals fulfill the all convergence criteria presented in Table 1 at the same time.

structures however, neither of the two ideal cases is well suited for inner grain boundaries, since they typically show an intermediate level of resistance against slip transmission. Such micro-flexible boundary conditions for gradient-enhanced crystal plasticity are for example discussed in Ekh et al. (2011) and Husser et al. (2017).

7.2. Effect of micromorphic penalty parameter

The micromorphic phase-field formulation adopts a penalty parameter $\alpha = \beta\, \mathcal{G}_0^{\mathrm{d}}/\ell_0$. Bharali et al. (2023) have shown for linear elastic problems that insufficient penalization leads to premature failure of the specimen (since the formulation turns into a local damage model in this case). For the chosen model problem, we have observed that the reaction force response is relatively robust against the choice of penalty parameter, but shows the same tendency of premature failure for very low choices of β. The lower sensitivity in our case can largely be attributed to the influence of plasticity in the proposed model. Fig. 5 displays the effect of drastically reducing the micromorphic penalty parameter β. Micro-free boundary conditions have been applied in these simulations. The resulting effect of a lower β is a decoupling of the local phase-field φ and the global phase-field d (as expected, compare Eq. (26)). While both phase-fields show a similar shape and magnitude for $\beta = 100$, the global phase-field d has much lower values and lacks localization for $\beta = 0.01$. In contrast, the local phase-field over-localizes for an insufficient penalty parameter in this example. The reason for this lack of regularization is that the local phase-field φ develops due to the increase of accumulated plastic strain ϵ^{p} in this case, it is mostly uninfluenced by the global phase-field d. This means that the effect of crack regularization inherent to phase-field fracture modeling, which occurs in the global equation system (compare Eq. (35)), does not permeate to the local problem described in Eq. (29), which determines φ. It should be noted that gradient-enhanced plasticity represents a regularization of the plastic strain field and that the response for an insufficiently penalized micromorphic phase-field model without gradient-enhanced plasticity shows even more pathological localization.

7.3. Damage irreversibility

In the presented model, damage irreversibility is ensured by introducing a history variable for the local phase-field, compare Section 4. In order to demonstrate the behavior of this formulation, the I-shaped specimen is loaded in a ratcheting manner, whereby the loading rate of $0.1\, L\,/\,t^*$ is kept from the previous numerical example. The loading curve is shown in the bottom right panel of Fig. 6. In addition to the previous set-up, two inhomogeneities are added to the I-shaped specimen at positions $\boldsymbol{X}_{\mathrm{c1}} = [0.45\, L,\ 0.83125\, L]$ and $\boldsymbol{X}_{\mathrm{c2}} = [0.2\, L,\ 0.7875\, L]$. The inhomogeneities are introduced by smoothly reducing the yield limit in the vicinity of the points $\boldsymbol{X}_{ci}$ by up to 95%, such that the effective yield limit is

$$\tau_{\mathrm{y,red}} = \left(1 - 0.95\, \mathrm{b}\left(\frac{|\boldsymbol{X} - \boldsymbol{X}_{ci}|}{r_{\mathrm{red}}}\right)\right)\tau_{\mathrm{y}}\,, \tag{51}$$

where b is a bump function

$$\mathrm{b}(x) = 1 - \frac{\exp(-1/x)}{\exp(-1/x) + \exp(-1/(1-x))}\,. \tag{52}$$

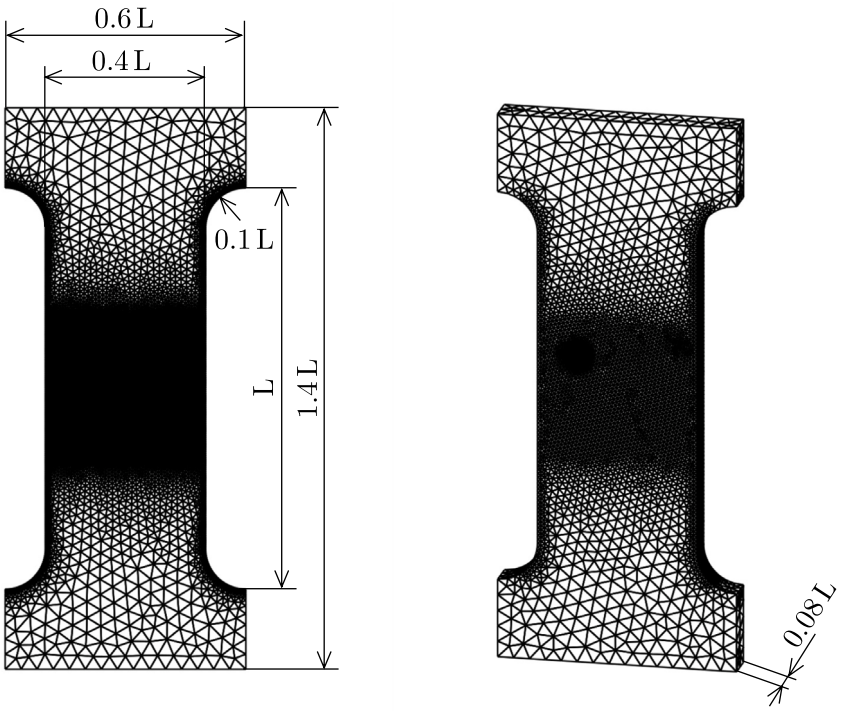

Fig. 2. Meshes for the 2D (left) and 3D (right) numerical examples. The cross-sectional geometry of the 3D-example is the same as for the 2D-example and geometrical measures are given in mm. Both examples employ unstructured meshes with a background element size of $0.04\,L$ and mesh refinements at the sides and in the center of the web, where the sample is expected to break. The refinements in the 2D-mesh consist of elements with an average size of $0.005\,L$, resulting in 19 390 linear triangular elements in total. In the 3D-mesh, center and sides employ elements of $0.01\,L$ average size and two positions are additionally refined with elements of $0.005\,L$ on average for imposing initial material inhomogeneities. The 3D mesh consists of 123 183 linear tetrahedral elements in total.

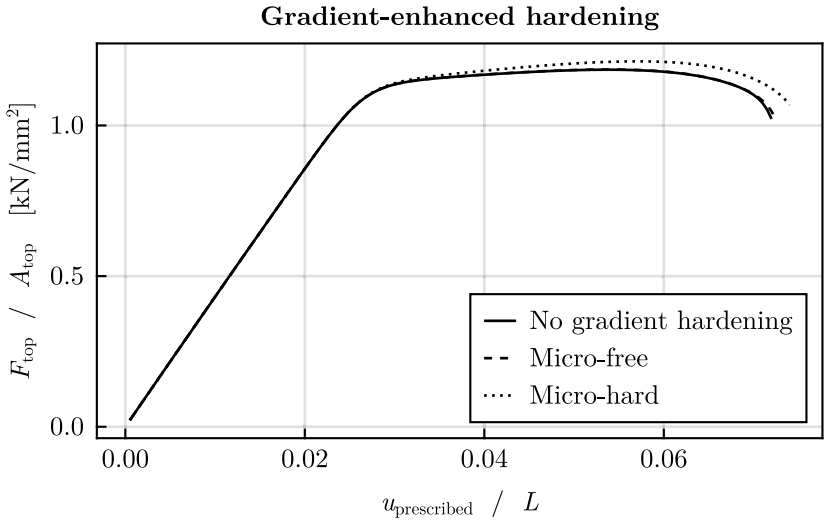

Fig. 3. Reaction force response for the I-shaped beam exposed to different boundary conditions, as well as without gradient hardening ($l^g = 0.0\,L$). All scenarios reach the softening regime. The micro-hard restriction of slip transfer on the boundaries leads to a stiffer response in the hardening regime. The last point of the curves corresponds to the last converged time step of the respective simulations.

A radius $r_{\text{red}} = 0.04\,L$ is chosen for the inhomogeneities and the mesh is refined with an average element size of $0.0025\,L$ within this radius around the points $\boldsymbol{X}_{ci}$. The left part of Fig. 6 shows the degradation g_e at the final step of the cyclic simulation. On the upper right of the figure, the resulting reaction forces from the cyclic loading and the equivalent monotonic loading are shown. On the lower right of the figure, the prescribed displacement together with the development of the local phase-field φ in a heavily degraded material point are shown. Within the first two cycles elastic loading and unloading are observed. During the subsequent cycles damage starts to develop in the vicinity of the inhomogeneities, which has an impact on the global reaction force curve. A noticeable viscous impact can be observed from the reaction force response around the load reversals and when comparing to the reaction force resulting from monotonic loading. The local phase-field history in the chosen integration point is displayed in the bottom right graph of Fig. 6. It begins to develop after 4 cycles. The phase-field grows during progressive loading, but remains constant during unloading and reloading. The same behavior can be observed for the degradation g_e and the global phase-field d. The obtained crack pattern shows a clear influence of the circular inhomogeneities. The diamond-shaped crack pattern observed in the previous numerical examples is disrupted and

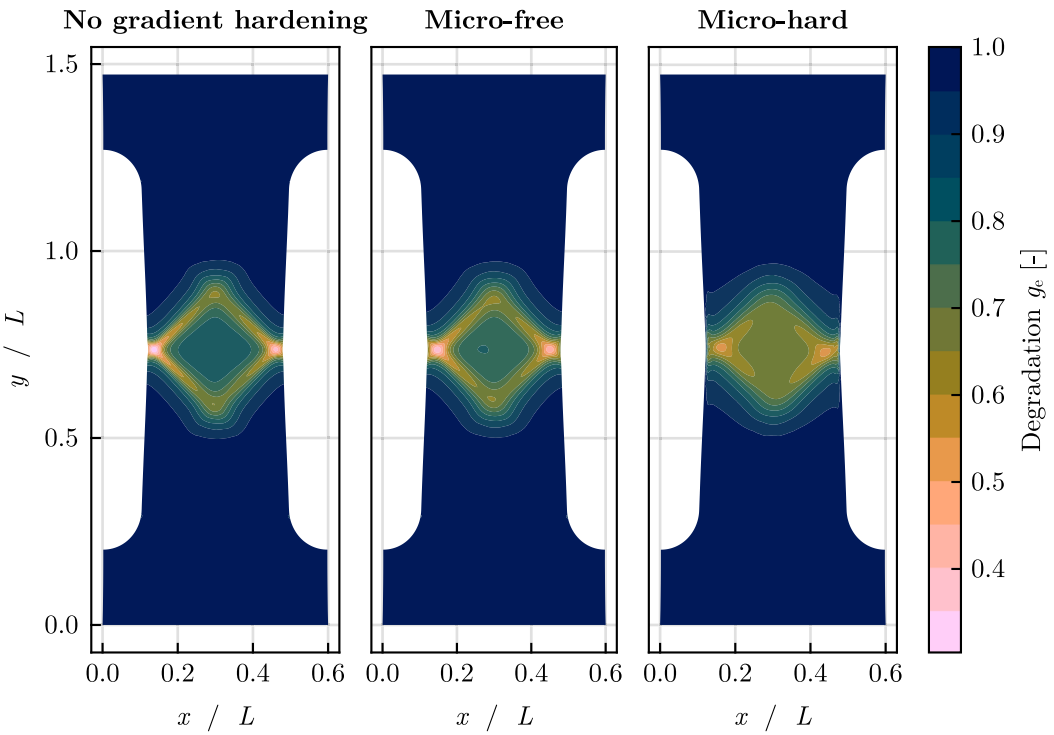

Fig. 4. Degradation g_e at the final step of the three base scenarios. The well known diamond shape crack pattern (compare e.g. De Lorenzis et al. (2016)) is recovered without gradient hardening. The behavior under micro-free boundary conditions is similar, but shows some smoothing of the crack shape. Under micro-hard boundary conditions plastic strains cannot develop on the boundary, thereby preventing the development of damage on the boundary.

instead a zig-zag shaped crack pattern results from the slip system orientation in conjunction with the inhomogeneities.

7.4. 3D simulation

A final simulation is conducted in order to display the capability of the model and numerical implementation to capture crack fronts in three dimensional space. The I-shaped specimen is extruded to a thickness of 0.08 L. Following Eqs. (51) and (52), spherical inhomogeneities are introduced at positions $\boldsymbol{X}_{c1} = [0.45\,L,\ 0.83125\,L,\ 0.05\,L]$ and $\boldsymbol{X}_{c2} = [0.2\,L,\ 0.7875\,L,\ 0.03\,L]$. Thereby a through-thickness inhomogeneous response is expected. Micro-free boundary conditions are applied and the phase-field length scale is set to $\ell_0 = 0.02\,L$. Fig. 7 displays the degradation g_e at the final step of the simulation from the front and the back side of the sample. For degradation values below 0.4, the material is assumed to be fractured and is displayed as transparent in Fig. 7. While the overall degradation response is comparable to that from the similar 2D cyclic simulation, differences in the crack patterns on the front and back side of the sample can be observed. A three-dimensional crack front develops, resulting from the two inhomogeneities placed at different through-thickness positions.

8. Concluding remarks

We have presented a thermodynamical framework that incorporates gradient-enhanced crystal plasticity in conjunction with a ductile phase-field fracture model in a large deformation setting. While the framework allows different approaches to incorporate damage irreversibility, this work puts the major focus on testing a recently suggested variationally and thermodynamically consistent micromorphic formulation, that allows for a localized phase-field formulation and enforces the irreversibility constraint on an integration point level. A prototype model is introduced for performing numerical experiments of the presented framework. It adopts an AT2-type of phase-field model which gives ductile fracture behavior by the choice of degradation function. The gradient-enhanced crystal plasticity model in conjunction with the micromorphic phase-field formulation and the ductile (plastic-strain based) degradation function leads to local equation systems that involve full coupling between local variables pertaining to the equilibrium equations as well as to the phase-field equation. Therefore, a staggered solution scheme that extends the global staggered solution scheme to the local level is presented and adopted. In the numerical examples, we demonstrate the effect that gradient-enhanced plasticity and the associated boundary conditions have on the fracture response. It is shown how the micromorphic phase-field formulation relies on sufficient penalization of the difference between the global and the local phase-fields. For insufficient penalization, the model turns into a local damage model and suffers from the associated drawbacks. Further, our numerical examples display that the presented model predicts unloading and reloading in a physically meaningful manner. The degradation of the material remains constant during unloading and advances once reloading goes past the previous level. Finally, the cyclic and the 3D experiments show that the model is able to account for material inhomogeneities and the resulting (arbitrary) crack patterns.

The presented work opens up for future investigation of polycrystalline fracture, where the authors in particular are interested in investigating the effect of grain boundaries in polycrystalline transgranular fracture. The presented gradient-extended crystal plasticity model allows to study the interaction between slip transfer at grain boundaries and crack propagation, as well as the impact of size effects in crack formation on the micro-scale. An essential feature for employing the model for the study of grain boundary effects in polycrystals is to define micro-flexible boundary conditions which interact with the phase-field fracture. In order to study crack propagation, solution schemes that allow to trace unstable crack growth, such as arc-length schemes (Bharali et al., 2022; Börjesson et al., 2022), and strategies to address convergence problems in the local equations systems are deemed important.

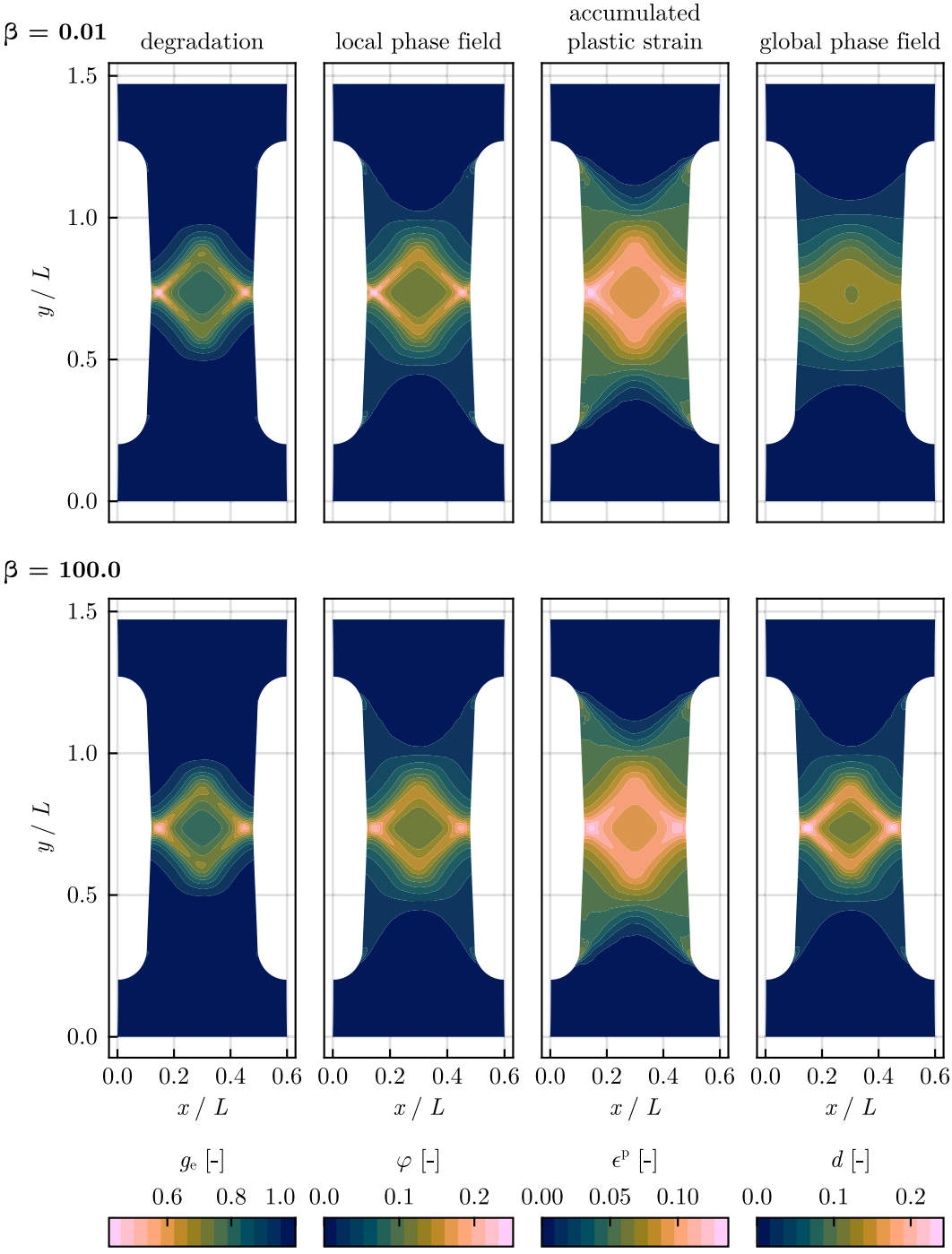

Fig. 5. Effect of the micromorphic penalty parameter β: The top row shows results for a low penalty effect, the bottom row shows results for a sufficient penalty effect. If the penalty parameter is chosen too low a decoupling between the global and the local phase-field occurs, resulting in a *lack* of regularization of the local phase-field φ. In this case the local phase-field φ is almost exclusively driven by the accumulated plastic strain ϵ^p, which leads to a high level of localization in the local phase-field. The global phase-field d instead experiences a lack of localization, as the coupling to the local phase-field φ decreases.

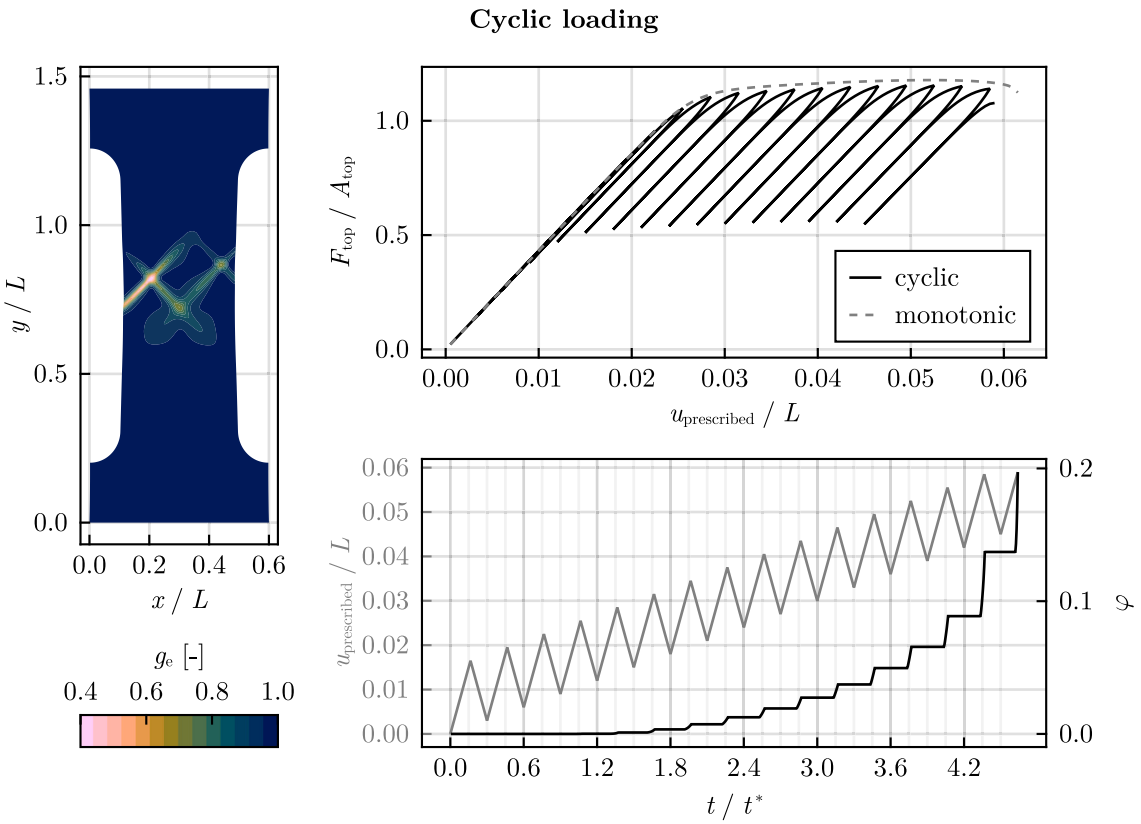

Fig. 6. Damage irreversibility can be observed under ratcheting loading. The I-shaped specimen with inhomogeneities is loaded under ratcheting loading in displacement control. Elastic unloading and reloading with a visible viscous impact can be observed in the reaction force response (top right). The prescribed loading curve and the development of the local phase-field φ in a specific material point are shown on the bottom right. After the initial elastic phase the local phase-field develops under advancing loading, but remains constant under unloading and reloading. The left plot shows the crack shape at the end of the simulation.

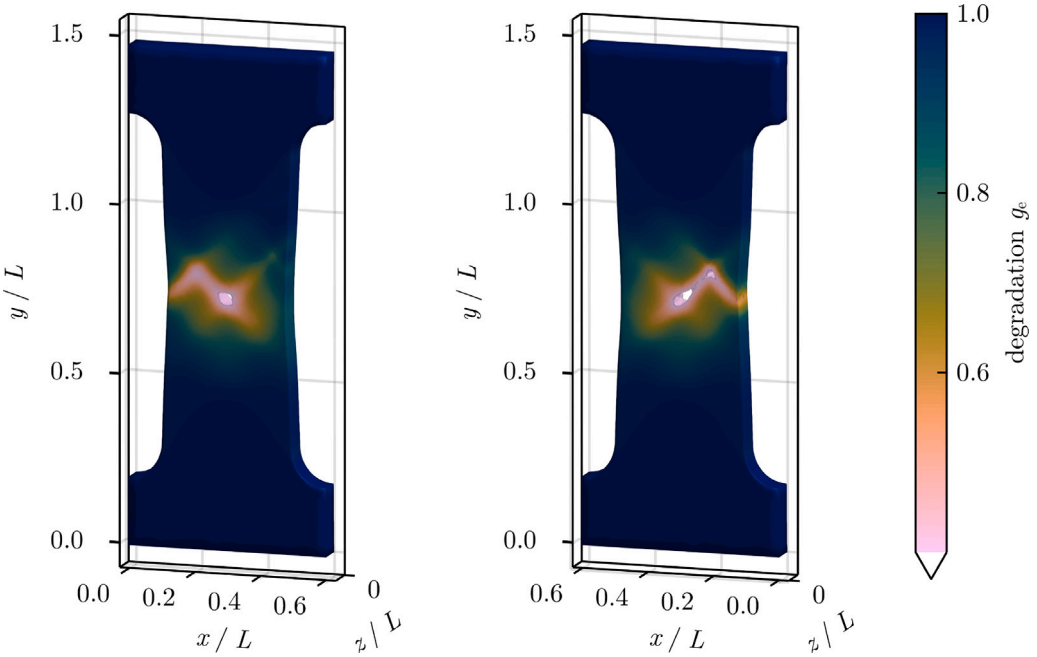

Fig. 7. Degradation g_e in the three-dimensional I-shaped specimen with two spherical inclusions at different through-thickness coordinates. Degradation values below 0.4 are displayed as crack. Distinct crack patterns evolve on the front (left plot) and back (right plot) side of the specimen, highlighting the three-dimensional nature of the crack.

Table 2
Base material parameters employed for the numerical experiments. L is a global length scale for the simulated structure and results are independent of L upon scaling according to Section 6.2.

Parameter		Value	Unit
Bulk modulus	κ	71 660	MPa
Shear modulus	μ	27 260	MPa
Yield stress	τ^{y}	345	MPa
Isotropic hardening modulus	H_{iso}	250	MPa
Gradient hardening modulus	H^{g}	1000	MPa
Gradient hardening length scale	l^{g}	$0.04\,L$	
Visco-plastic relaxation time	t^*	1	s
Visco-plastic drag stress	σ^{d}	500	MPa
Visco-plastic exponent	m	8	–
Effective fracture energy	$\mathcal{G}_0^{\mathrm{d}}/\ell_0$	300	N/mm^2
Phase-field length scale	ℓ_0	$0.005\,L$	
Micromorphic penalty parameter	α	$200\,\mathcal{G}_0^{\mathrm{d}}/\ell_0$	
Critical plastic strain	$\epsilon^{\mathrm{p}}_{\mathrm{crit}}$	0.1	–
Degradation exponent	n	2	–

Table 3
FCC slip systems. The unit cell is aligned with the coordinate axes in the numerical examples. In the numerical examples slip systems 2, 5, 8, 11 are omitted, because they are perpendicular to the loading direction and have a negligible impact on the plastification process. In the cyclic and the 3D example, only the 4 slip systems with the largest impact are used, that is slip systems 1, 4, 7, 10.

α	$\bar{\mathbf{s}}_\alpha$	$\bar{\mathbf{m}}_\alpha$	α	$\bar{\mathbf{s}}_\alpha$	$\bar{\mathbf{m}}_\alpha$	α	$\bar{\mathbf{s}}_\alpha$	$\bar{\mathbf{m}}_\alpha$	α	$\bar{\mathbf{s}}_\alpha$	$\bar{\mathbf{m}}_\alpha$
1	$[\bar{1}\,1\,0]$	$[1\,1\,1]$	4	$[\bar{1}\,\bar{1}\,0]$	$[1\,\bar{1}\,\bar{1}]$	7	$[1\,1\,0]$	$[\bar{1}\,1\,\bar{1}]$	10	$[1\,\bar{1}\,0]$	$[\bar{1}\,\bar{1}\,1]$
2	$[1\,0\,\bar{1}]$	$[1\,1\,1]$	5	$[1\,0\,1]$	$[1\,\bar{1}\,\bar{1}]$	8	$[\bar{1}\,0\,1]$	$[\bar{1}\,1\,\bar{1}]$	11	$[\bar{1}\,0\,\bar{1}]$	$[\bar{1}\,\bar{1}\,1]$
3	$[0\,\bar{1}\,1]$	$[1\,1\,1]$	6	$[0\,1\,\bar{1}]$	$[1\,\bar{1}\,\bar{1}]$	9	$[0\,\bar{1}\,\bar{1}]$	$[\bar{1}\,1\,\bar{1}]$	12	$[0\,1\,1]$	$[\bar{1}\,\bar{1}\,1]$

CRediT authorship contribution statement

Kim Louisa Auth: Writing – review & editing, Writing – original draft, Visualization, Validation, Software, Project administration, Methodology, Investigation, Data curation. **Jim Brouzoulis:** Writing – review & editing, Supervision. **Magnus Ekh:** Writing – review & editing, Writing – original draft, Validation, Supervision, Project administration, Methodology, Funding acquisition, Conceptualization.

Declaration of competing interest

The authors declare that they have no known competing financial interests or personal relationships that could have appeared to influence the work reported in this paper.

Data availability

Data will be made available on request.

Acknowledgment

The work in this paper has been funded by the Swedish Research Council (Vetenskapsrådet) under the grant number 2018-04318.

Appendix A. Material parameters

See Tables 2 and 3.

Appendix B. Microforce derivation

An alternative derivation of the gradient-extended plasticity and the phase-field following the procedure in Borden et al. (2018) is summarized here in point-form.

- Microforce balances

$$\boldsymbol{\nabla}_0 \cdot \boldsymbol{\xi}_\alpha + \pi_\alpha + l_\alpha = 0 \tag{53}$$

$$\boldsymbol{\nabla}_0 \cdot \boldsymbol{\xi}_d + \pi_d + l_d = 0 \tag{54}$$

with $l_\alpha = l_d = 0$.

- Dissipation inequality

$$\boldsymbol{P} : \dot{\boldsymbol{F}} + \sum_{\alpha=1}^{n_\alpha} \boldsymbol{\xi}_\alpha \cdot \boldsymbol{\nabla}_0 \dot{k}_\alpha - \sum_{\alpha=1}^{n_\alpha} \pi_\alpha\, \dot{k}_\alpha + \boldsymbol{\xi}_d \cdot \boldsymbol{\nabla}_0 \dot{d} - \pi_d\, \dot{d} - \dot{\Psi} \geq 0 \tag{55}$$

- Free energy

$$\Psi = \Psi\left(\boldsymbol{C}_{\mathrm{e}},\, q,\, \{k_\alpha\}_{\alpha=1}^{n_\alpha},\, \{\boldsymbol{\nabla}_0 k_\alpha\}_{\alpha=1}^{n_\alpha},\, d,\, \boldsymbol{\nabla}_0 d\right) \tag{56}$$

gives

$$\boldsymbol{S}_{\mathrm{e}} = 2\,\frac{\partial \Psi}{\partial \boldsymbol{C}_{\mathrm{e}}} \tag{57}$$

and the reduced dissipation inequality

$$\begin{aligned} \mathcal{D} = {} & \boldsymbol{M}_{\mathrm{e}} : \boldsymbol{L}_{\mathrm{p}} + Q\,\dot{q} - \sum_{\alpha=1}^{n_\alpha} \left(\frac{\partial \Psi}{\partial k_\alpha} + \pi_\alpha \right) \dot{k}_\alpha \\ & - \sum_{\alpha=1}^{n_\alpha} \left(\frac{\partial \Psi}{\partial \boldsymbol{\nabla}_0 k_\alpha} - \boldsymbol{\xi}_\alpha \right) \cdot \boldsymbol{\nabla}_0 \dot{k}_\alpha \\ & - \left(\frac{\partial \Psi}{\partial d} + \pi_d \right) \dot{d} - \left(\frac{\partial \Psi}{\partial \boldsymbol{\nabla}_0 d} - \boldsymbol{\xi}_d \right) \cdot \boldsymbol{\nabla}_0 \dot{d} \geq 0 \end{aligned} \tag{58}$$

- By assuming $\boldsymbol{\xi}_\alpha$, π_d and $\boldsymbol{\xi}_d$ energetic, i.e.

$$\boldsymbol{\xi}_\alpha = \frac{\partial \Psi}{\partial \boldsymbol{\nabla}_0 k_\alpha}, \quad \pi_d = -\frac{\partial \Psi}{\partial d}, \quad \boldsymbol{\xi}_d = \frac{\partial \Psi}{\partial \boldsymbol{\nabla}_0 d} \tag{59}$$

gives

$$\boldsymbol{M}_{\mathrm{e}} : \boldsymbol{L}_{\mathrm{p}} + Q\,\dot{q} + \sum_{\alpha=1}^{n_\alpha} \kappa_\alpha\, \dot{k}_\alpha \geq 0 \tag{60}$$

where

$$\kappa_\alpha = -\frac{\partial \Psi}{\partial k_\alpha} + \boldsymbol{\nabla}_0 \cdot \frac{\partial \Psi}{\partial \boldsymbol{\nabla}_0 k_\alpha} \tag{61}$$

by using the microforce balance. This is identical to $Y_\alpha = 0$ in (7).

- Insert π_d and $\boldsymbol{\xi}_d$ into microforce balance

$$\boldsymbol{\nabla}_0 \cdot \frac{\partial \Psi}{\partial \boldsymbol{\nabla}_0 d} - \frac{\partial \Psi}{\partial d} = 0 \tag{62}$$

which is identical to $Y = 0$ in (9).

References

Alessi, Roberto, Marigo, Jean Jacques, Vidoli, Stefano, 2015. Gradient damage models coupled with plasticity: Variational formulation and main properties. Mech. Mater. (ISSN: 01676636) 80 (PB), 351–367. http://dx.doi.org/10.1016/j.mechmat.2013.12.005.

Alessi, R., et al., 2018. Comparison of phase-field models of fracture coupled with plasticity. In: Computational Methods in Applied Sciences. Vol. 46, (ISSN: 18713033) ISBN: 9783319608853, pp. 1–21. http://dx.doi.org/10.1007/978-3-319-60885-3{_}1.

Ambati, M., Gerasimov, T., De Lorenzis, L., 2015. Phase-field modeling of ductile fracture. Comput. Mech. (ISSN: 01787675) 55 (5), 1017–1040. http://dx.doi.org/10.1007/s00466-015-1151-4.

Ambrosio, Luigi, Tortorelli, Vincenzo Maria, 1990. Approximation of functional depending on jumps by elliptic functional via Gamma-convergence. Comm. Pure Appl. Math. (ISSN: 10970312) 43 (8), 999–1036. http://dx.doi.org/10.1002/cpa.3160430805.

Aslan, O., et al., 2011. Micromorphic approach to single crystal plasticity and damage. Internat. J. Engrg. Sci. (ISSN: 00207225) 49 (12), 1311–1325. http://dx.doi.org/10.1016/j.ijengsci.2011.03.008.

Bargmann, Swantje, et al., 2010. Modeling of polycrystals with gradient crystal plasticity: A comparison of strategies. Phil. Mag. (ISSN: 14786435) 90 (10), 1263–1288. http://dx.doi.org/10.1080/14786430903334332.

Bezanson, Jeff, et al., 2017. Julia: A fresh approach to numerical computing. SIAM Rev. (ISSN: 00361445) 59 (1), 65–98. http://dx.doi.org/10.1137/141000671.

Bharali, Ritukesh, Larsson, Fredrik, Jänicke, Ralf, 2023. A micromorphic phase-field model for brittle and quasi-brittle fracture. Comput. Mech. (ISSN: 14320924) http://dx.doi.org/10.1007/s00466-023-02380-1.

Bharali, Ritukesh, et al., 2022. A robust monolithic solver for phase-field fracture integrated with fracture energy based arc-length method and under-relaxation. Comput. Methods Appl. Mech. Engrg. (ISSN: 00457825) 394, 114927. http://dx.doi.org/10.1016/j.cma.2022.114927.

Borden, Michael J, et al., 2018. Phase-field formulation for ductile fracture. In: Advances in Computational Plasticity: A Book in Honour of D. Roger J. Owen. Springer, pp. 45–70.

Börjesson, Elias, Remmers, Joris J.C., Fagerström, Martin, 2022. A generalised path-following solver for robust analysis of material failure. Comput. Mech. (ISSN: 14320924) 70 (2), 437–450. http://dx.doi.org/10.1007/s00466-022-02175-w.

Bourdin, Blaise, Francfort, Gilles A., Marigo, Jean Jacques, 2008. The variational approach to fracture. J. Elasticity (ISSN: 03743535) 91 (1–3), 5–148. http://dx.doi.org/10.1007/s10659-007-9107-3.

Carlsson, Kristoffer, Ekre, Fredrik, 2019. Tensors.jl - Tensor computations in Julia. J. Open Res. Softw. (ISSN: 20499647) 7 (1), 2–6. http://dx.doi.org/10.5334/jors.182.

Carlsson, Kristoffer, Ekre, Fredrik, Contributors, Ferrite.jl - Finite element toolbox for Julia. URL: https://github.com/Ferrite-FEM/Ferrite.jl.

Carlsson, Kristoffer, et al., 2017. A comparison of the primal and semi-dual variational formats of gradient-extended crystal inelasticity. Comput. Mech. (ISSN: 01787675) 60 (4), 531–548. http://dx.doi.org/10.1007/s00466-017-1419-y.

Coleman, Bernard D., Noll, Walter, 1963. The thermodynamics of elastic materials with heat conduction and viscosity. Arch. Ration. Mech. Anal. 13, 167–178. http://dx.doi.org/10.1007/BF01262690.

Danisch, Simon, Krumbiegel, Julius, 2021. Makie.jl: Flexible high-performance data visualization for Julia. J. Open Source Softw. 6 (65), 3349. http://dx.doi.org/10.21105/joss.03349.

De Borst, René, Pamin, Jerzy, Geers, Marc G.D., 1999. On coupled gradient-dependent plasticity and damage theories with a view to localization analysis. Eur. J. Mech. A Solids (ISSN: 09977538) 18 (6), 939–962. http://dx.doi.org/10.1016/S0997-7538(99)00114-X.

De Lorenzis, Laura, Gerasimov, Tymofiy, 2020. Numerical implementation of phase-field models of brittle fracture. In: De Lorenzis, Laura, Düster, Alexander (Eds.), Modeling in Engineering using Innovative Numerical Methods for Solids and Fluids. Springer, Udine, pp. 75–101.

De Lorenzis, L., McBride, A., Reddy, B.D., 2016. Phase-field modelling of fracture in single crystal plasticity. GAMM-Mitt. (ISSN: 09367195) 39 (1), 7–34. http://dx.doi.org/10.1002/gamm.201610002.

Dimitrijevic, B.J., Hackl, K., 2011. A regularization framework for damage–pla sticity models via gradient enhancement of the free energy. Int. J. Numer. Methods Biomed. Eng. (ISSN: 2040-7939) 27 (8), 1149–1320. http://dx.doi.org/10.1002/cnm.1350.

Ekh, Magnus, Bargmann, Swantje, Grymer, Mikkel, 2011. Influence of grain boundary conditions on modeling of size-dependence in polycrystals. Acta Mech. (ISSN: 00015970) 218 (1–2), 103–113. http://dx.doi.org/10.1007/s00707-010-0403-9.

Ekh, Magnus, Lillbacka, Robert, Runesson, Kenneth, 2004. A model framework for anisotropic damage coupled to crystal (visco)plasticity. Int. J. Plast. (ISSN: 07496419) 20 (12), 2143–2159. http://dx.doi.org/10.1016/j.ijplas.2004.04.007.

Ekh, Magnus, et al., 2007. Gradient crystal plasticity as part of the computational modelling of polycrystals. Internat. J. Numer. Methods Engrg. 72 (2), 197–220. http://dx.doi.org/10.1002/nme.2015.

Evers, L.P., Brekelmans, W.A.M., Geers, M.G.D., 2004. Scale dependent crystal plasticity framework with dislocation density and grain boundary effects. Int. J. Solids Struct. (ISSN: 00207683) 41 (18–19), 5209–5230. http://dx.doi.org/10.1016/j.ijsolstr.2004.04.021.

Flouriot, S., et al., 2003. Strain localization at the crack tip in single crystal CT specimens under monotonous loading: 3D finite element analyses and application to nickel-base superalloys. Int. J. Fract. (ISSN: 03769429) 124 (1–2), 43–77. http://dx.doi.org/10.1023/B:FRAC.0000009300.70477.ba.

Forest, Samuel, 2009. Micromorphic approach for gradient elasticity, viscoplasticity, and damage. J. Eng. Mech. (ISSN: 0733-9399) 135 (3), 117–131. http://dx.doi.org/10.1061/(asce)0733-9399(2009)135:3(117).

Gerasimov, T., De Lorenzis, L., 2019. On penalization in variational phase-field models of brittle fracture. Comput. Methods Appl. Mech. Engrg. (ISSN: 00457825) 354, 990–1026. http://dx.doi.org/10.1016/j.cma.2019.05.038.

Gurtin, Morton E., 2002. A gradient theory of single-crystal viscoplasticity that accounts for geometrically necessary dislocations. J. Mech. Phys. Solids (ISSN: 00225096) 50 (1), 5–32. http://dx.doi.org/10.1016/S0022-5096(01)00104-1.

Hernandez Padilla, Carlos Alberto, Markert, Bernd, 2014. A coupled phase-field model for ductile fracture in crystal plasticity. Pamm (ISSN: 16177061) 14 (AUGUST), 441–442. http://dx.doi.org/10.1002/pamm.201410208, URL: http://doi.wiley.com/10.1002/pamm.201410208.

Husser, Edgar, Soyarslan, Celal, Bargmann, Swantje, 2017. Size affected dislocation activity in crystals: Advanced surface and grain boundary conditions. Extreme Mech. Lett. (ISSN: 23524316) 13, 36–41. http://dx.doi.org/10.1016/j.eml.2017.01.007.

Maloth, Thirupathi, Ghosh, Somnath, 2023. Coupled crystal plasticity phase-field model for ductile fracture in polycrystalline microstructures. Int. J. Multiscale Comput. Eng. (ISSN: 15431649) 21 (2), 1–19. http://dx.doi.org/10.1615/IntJMultCompEng.2022042164.

Miehe, Christian, Aldakheel, Fadi, Teichtmeister, Stephan, 2017. Phase-field modeling of ductile fracture at finite strains: A robust variational-based numerical implementation of a gradient-extended theory by micro. Internat. J. Numer. Methods Engrg. 111 (9), 816–863. http://dx.doi.org/10.1002/nme.5484, URL: https://onlinelibrary.wiley.com/doi/10.1002/nme.5484.

Miehe, Christian, Hofacker, Martina, Welschinger, Fabian, 2010a. A phase field model for rate-independent crack propagation: Robust algorithmic implementation based on operator splits. Comput. Methods Appl. Mech. Engrg. (ISSN: 00457825) 199 (45–48), 2765–2778. http://dx.doi.org/10.1016/j.cma.2010.04.011.

Miehe, Christian, Welschinger, F., Hofacker, M., 2010b. Thermodynamically consistent phase-field models of fracture: Variational principles and multi-field FE implementations. Internat. J. Numer. Methods Engrg. 83, 1273–1311. http://dx.doi.org/10.1002/nme.2861.

Rovinelli, Andrea, et al., 2018. Using machine learning and a data-driven approach to identify the small fatigue crack driving force in polycrystalline materials. Npj Comput. Mater. (ISSN: 20573960) 4 (1), 1–10. http://dx.doi.org/10.1038/s41524-018-0094-7.

Simo, J.C., 1988. A framework for finite strain elastoplasticity based on maximum plastic dissipation and the multiplicative decomposition: Part 1. Continuum formulation. Comput. Methods Appl. Mech. Engrg. 66 (2), 199–219.

Svedberg, Thomas, Runesson, Kenneth, 1998. An algorithm for gradient-regularized plasticity coupled to damage based on a dual mixed FE-formulation. Comput. Methods Appl. Mech. Engrg. (ISSN: 0346718X) 161 (1–2), 49–65. http://dx.doi.org/10.1016/S0045-7825(97)00309-5, URL: https://www.sciencedirect.com/science/article/pii/S0045782597003095?via%3Dihub.